Atom Indonesia

Journal homepage: http://atomindonesia.brin.go.id

Comparison of Lung Cancer Lesion Detection Capability on Standard Dose and Low Dose Computed Tomography Capabilities: An In-House Phantom Study

A. K. Hutami[1*], H. D. R. Rahaja[2], L. E. Lubis[1,3*], D. S. Soejoko[1]

[1]*Department of Physics, Faculty of Mathematics and Natural Sciences, Universitas Indonesia, Kampus UI, Depok 16424, Indonesia*
[2]*Department of Radiology, MRCCC Siloam Semanggi Hospital, Jakarta, 12930, Indonesia*
[3]*Radiology Unit, Universitas Indonesia Hospital, Universitas Indonesia, Kampus UI, Depok 16424, Indonesia*

ARTICLE INFO

Article history:
Received 20 December 2024
Received in revised form 18 March 2025
Accepted 4 May 2025

Keywords:

Low-dose computed tomography
Phantom in-house
Signal difference to noise ratio
Figure of merit
Noise power spectrum

ABSTRACT

The use of Low-Dose Computed Tomography (LDCT) protocols has garnered significant attention, particularly in detecting cancerous lesions in high-risk populations. However, the drawback of low-dose CT protocols results in image noise. Solutions introduced, such as the use of reconstruction techniques, tend to be time-inefficient, complex, and costly. This paper aims to explain the design and construction of an approach for evaluating the quality of lung cancer lesion imaging that is adequate and easily implementable. In this study, a custom-designed in-house phantom is required to simulate lung cancer lesions. The in-house phantom was constructed from organ or tissue-equivalent materials and equipped with various Hounsfield Unit values and lesion diameter sizes, which were determined based on data from 73 patients, consisting of both males and females, using contrast. Scans were performed on the phantom using standard-dose and low-dose protocol parameters. The results demonstrated that the low-dose protocol was able to detect small lesions at lower radiation levels. The contrast difference is quite good with a Signal Difference to Noise Ratio (SDNR) value ≥ 5. The image was optimum with a relatively high Figure of Merit (FOM). Additionally, Noise Power Spectrum (NPS) measurements provided accurate results within a specific range of spatial frequencies.

INTRODUCTION

According to data published by the World Health Organization (WHO) in 2020, the cancer profile in Indonesia showed that in 2018, the total number of cancer-related deaths reached 207, 210. Lung cancer accounted for the highest mortality rate, contributing 12.6% of all cancer cases [1]. This has become a particular concern, prompting various efforts to reduce lung cancer mortality, one of which is through screening for lung cancer.

Lung cancer screening involves imaging techniques that rely on the modality's capability to detect cancerous lesions at an early stage. Chest computed tomography is widely used for assessing various abnormalities and disorders affecting the respiratory tract, mediastinum, and lungs. However, scans performed using computed tomography expose patients to harmful ionizing radiation. The amount of radiation delivered to patients during standard-dose protocols ranges from 4 to 7 mSv [2]. Recently, lung cancer screening programs using low-dose protocols have offered a more effective method for detecting early-stage cancer in high-risk populations. This is because screening tests are conducted on large populations and are repeated in healthy individuals [3-8]. According to the Biological Effects of Ionizing Radiation VII (BEIR VII) report, the lifetime risk of developing cancer due to radiation exposure from Low-Dose Computed Tomography (LDCT) procedures is relatively small, ranging from 0.01% to 0.06% [9]. However, reducing radiation dose in low-dose protocols can lead to lower specificity and higher noise [10].

*Corresponding author.
E-mail address: lukmanda.evan@sci.ui.ac.id
DOI: https://doi.org/10.55981/aij.2025.1587

To overcome these problems, various techniques have been proposed to optimize both image quality and radiation dose, such as the use of iterative reconstruction algorithms and Deep Learning Image Reconstruction (DLIR) in lung scans [11-14]. However, vendor-based strategies are often time-inefficient and expensive for routine use in hospitals. Therefore, this study proposes an alternative approach, more affordable and flexible for evaluating scan image quality, particularly when comparing standard-dose and low-dose protocols. One potential approach is the development of an in-house phantom designed with lesion-equivalent objects, where image quality and lesion detection performance in two scanning categories are evaluated.

METHODOLOGY

Phantom materials and design

The simulation of Hounsfield Unit values and lesion diameter sizes was based on the smallest value range in the distribution of lung cancer lesion data from 73 patients using contrast. The variations in Hounsfield Unit values include -500 HU, -400 HU, -300 HU, and -200 HU, with lesion diameters of 2 mm, 4 mm, 6 mm, and 8 mm.

The phantom material is primarily composed of polyurethane foam that resembles lung tissue, paraffin wax as a casing resembling soft tissue, and polyurethane resin [16]. A total of 16 insert objects were designed to be placed inside the phantom, with each insert consisting of four groups of holes with varying diameters. Each group is filled with a different composition of polyurethane resin and hardener to resemble the Hounsfield Unit values of lesions (Fig. 1).

(a) (b) (c)

Fig. 1. In-house Phantom Design. (a) Front, (b-c) Side Variations of Hounsfield and lesion diameter sizes.

Phantom scanning

The phantom was scanned using the Philips iBrilliance 256-Slice CT scanner. Scanning was performed with two protocols. First, the standard dose protocol used 120 kVp energy, 200 mAs tube current, a Field of View (FOV) of 250 mm, a rotation time of 0.5 seconds, a pitch of 0.993, and kernel B. Next, scanning was performed without interruption using the low-dose protocol with 120 kVp energy, tube currents of 10 mAs, 30 mAs, and 50 mAs, a Field of View (FOV) of 250 mm, a rotation time of 0.5 seconds, a pitch of 0.586, and kernel L.

In the computed tomography modality in this study, the B kernel is classified as a smooth kernel, while the L kernel is categorized as a sharp kernel. Kernel B is commonly used at the study site for standard-dose protocols.

For each protocol, variations in slice thickness were applied, specifically 1 mm, 2 mm, 3 mm, 4 mm, and 5 mm. Both protocols used the helical or spiral scanning mode. The parameters used in the standard dose protocol are routine protocols employed at the study site.

Image quality evaluation

In assessing the ability to differentiate between two different contrasts in the image, the Signal Difference to Noise Ratio (SDNR) parameter is calculated using Eq. (1) [15].

$$SDNR = \frac{|N_l - N_{o,i}|}{\sqrt{\frac{(STD^2{}_{o,i} + STD^2{}_l)}{2}}} \quad (1)$$

In Eq. 1, N_l represents the pixel value of the background, and $N_{o,\,i}$ represents the pixel value of the object. Meanwhile, $STD^2_{o,i}$ is the standard deviation of the object, and STD^2_l represents the standard deviation value of the background. The Region of Interest (ROI) is selected for both the object and the background, with the ROI area being larger than the object itself. The selection of the ROI begins with the slice that shows abnormalities from the total set of slices. However, this method is not used to obtain the NPS value.

A similar approach is used to determine the optimization of image quality and radiation dose, represented by the Figure of Merit (FOM) parameter, taking into account the noise level (SDNR) and the recorded dose of the scanning display Computed Tomography Dose Index Volume ($CTDI_{vol}$), as expressed in Eq. (2) [16].

$$FOM = \frac{SDNR^2}{CTDI_{vol}} \quad (2)$$

The final approach involves evaluating the phantom's capability as a tool for measuring advanced system quality metrics through the measurement of the Noise Power Spectrum (NPS),

which represents the amount of noise distribution within a frequency range. The NPS measurements were performed using the iQMetrik-CT software from the University of Sorbonne, following the user guide [17].

RESULTS AND DISCUSSION

Image quality evaluation

Signal Difference to Noise Ratio (SDNR)

In-house phantom scans of standard dose (200 mAs) and low-dose (10 mAs, 30 mAs, and 50 mAs) protocols are shown in Fig. 2. Since the primary goal of constructing the phantom was to develop a tool for evaluating the capability of standard-dose and low-dose protocols in detecting lung cancer lesions, the approach involved calculations of SDNR and FOM.

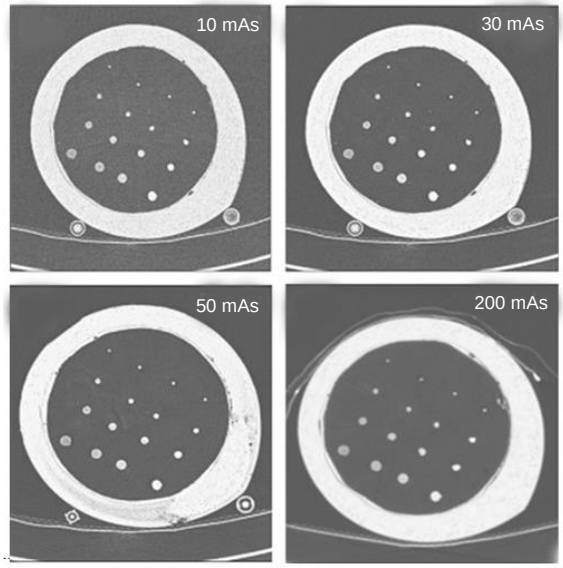

(a)

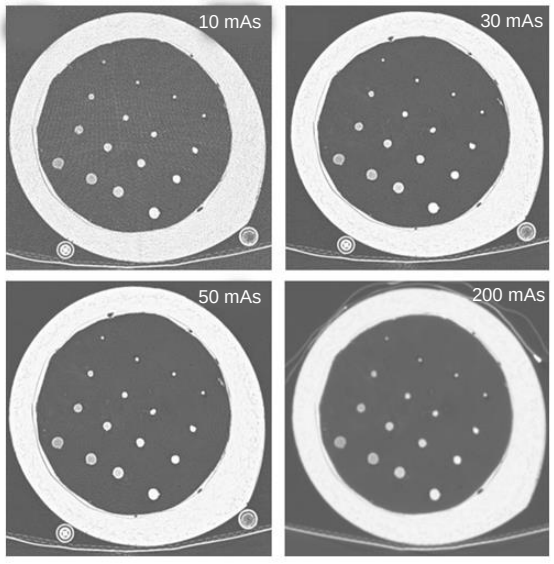

(b)

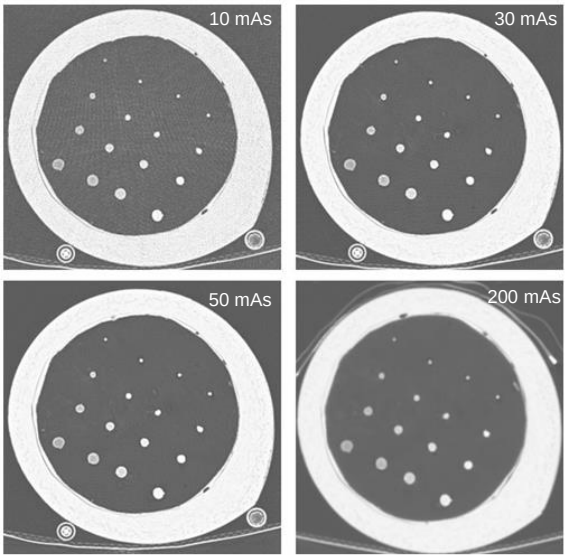

(c)

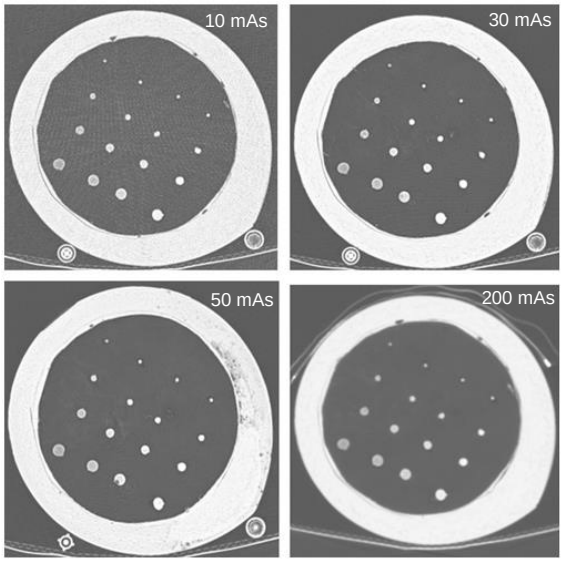

(d)

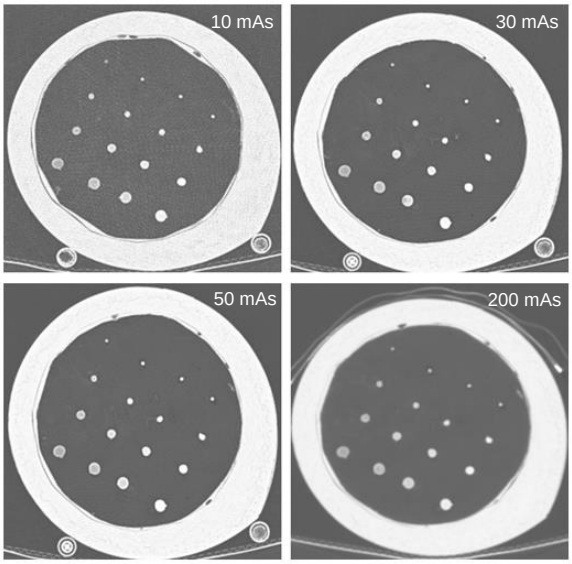

(e)

Fig. 2. Scan results at each slice thickness: (a) 1 mm, (b) 2 mm, (c) 3 mm, (d) 4 mm, and (e) 5 mm.

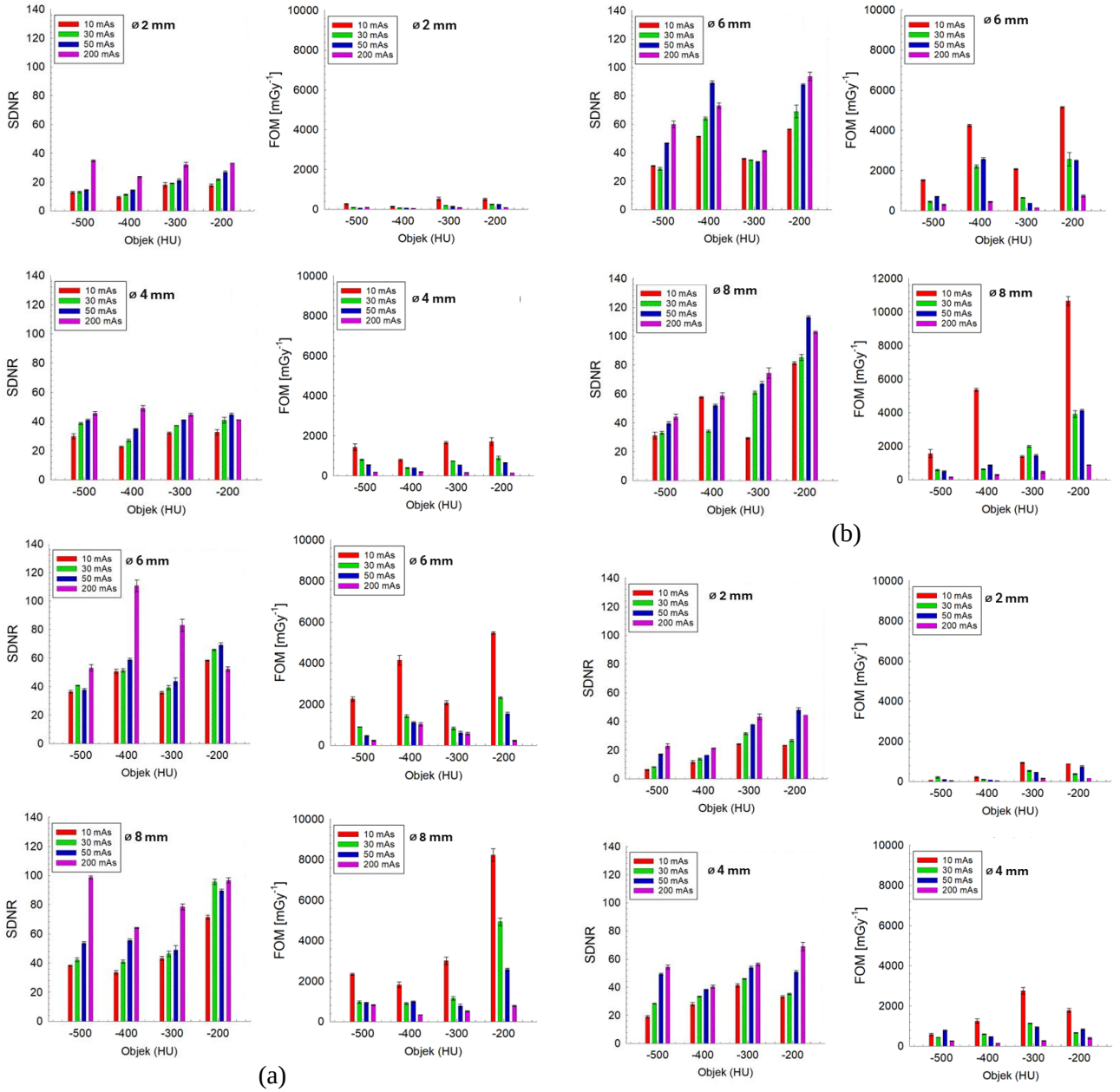
10 mAs
30 mAs
50 mAs
200 mAs
ø 2 mm
ø 4 mm
ø 6 mm
ø 8 mm
SDNR
FOM [mGy⁻¹]
Objek (HU)
-500
-400
-300
-200
(a)
(b)
(c)

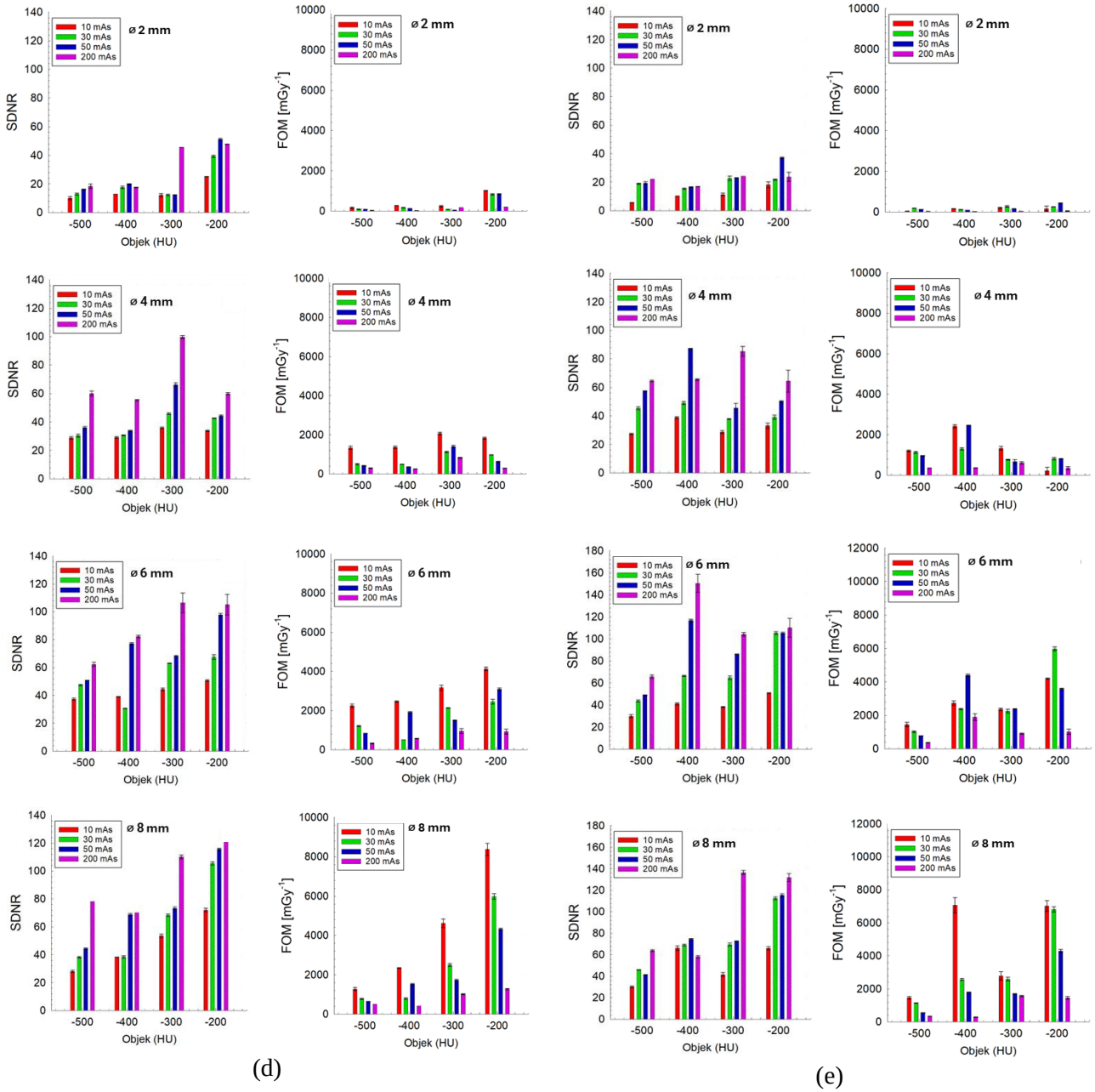

Fig. 3. Results of SDNR and FOM measurements for various slice thicknesses (a = 1 mm; b = 2 mm; c = 3 mm; d = 4 mm; and e = 5 mm).

In Fig. 2, the in-house phantom scan results at the standard dose (200 mAs) appear faint across various lesion diameters and slice thicknesses. However, quantitative analysis in Fig. 3 reveals that the highest overall SDNR is achieved with the standard dose. The discrepancy between visual assessment and SDNR calculations aligns with Rose's contrast model, which states that the human eye's visibility threshold is at SDNR = 5 [18].

Figure 3 also reveals that SDNR values increase with higher tube current, larger lesion diameters, and greater slice thickness. This indicates that low-dose imaging can still detect small objects. However, the highest SDNR values are consistently observed at the standard dose, as the higher tube current generates more X-ray photons, resulting in a stronger signal due to a greater number of photons reaching the detector [19].

According to chest guidelines and expert reports on lung cancer screening, summarized from randomized controlled trials, detectable lesions are typically ≥ 4 mm [20]. However, in this study, the smallest simulated lung cancer lesion was detectable.

Additionally, Fig. 3 reveals that objects with a Hounsfield Unit (HU) value greater than -500 HU (closer to soft tissue) tend to show an increasing trend as the lesion diameter increases. This is due to the significant HU difference between the object and the background. The ability of imaging

modalities to detect high-HU values is crucial for diagnosis. A study by Ichikawa et al. stated that higher HU values are easier to detect than lower HU values due to their distinctive subtle contrast [21]. In CT imaging, HU values help identify the nature of nodules or lesions based on density levels. A higher HU value indicates greater density, while a lower HU value indicates reduced density [22].

Figure of Merit (FOM)

Balancing image quality and radiation dose is essential in medical imaging. Tube current is directly proportional to the radiation dose received [23,24], making protocol optimization necessary to achieve this balance. The Figure of Merit (FOM) is a commonly used parameter. According to a study by Priyanka et al., FOM is derived from the Contrast-to-Noise Ratio (CNR) for image quality evaluation and CTDIvol for dose assessment [25].

In this study, FOM is calculated using Eq. (2), with results shown in Fig. 3. Figure 3 indicates that FOM tends to increase with larger lesion diameters, higher HU values, and greater slice thickness. It also reveals that the highest FOM is achieved at the lowest tube current (10 mAs). This is because the denominator in the FOM equation is the dose. Using the lowest tube current is beneficial for screening examinations requiring monitoring or repeated scans, as it results in a lower radiation dose and minimizes the risk of side effects.

Noise Power Spectrum (NPS)

The influence of slice thickness, kernel type, and mAs on NPS can be observed in Table 1. NPS is a function that describes the distribution of noise across a frequency range. As shown in Table 1, NPS values are affected by slice thickness and variations in mAs.

For 10 mAs, the frequency value ranges from 0.9 to 1.0 mm^{-1}, with noise values between 135 and 147 $HU^2 \cdot mm^2$. For 30 mAs, the frequency value ranges from 0.7 to 0.8 mm^{-1}, with noise values between 45 and 63 $HU^2 \cdot mm^2$. For 50 mAs, the frequency value also ranges from 0.7 to 0.8 mm^{-1}, with noise values between 40 and 54 $HU^2 \cdot mm^2$.

This indicates that a slice thickness of 1 mm provides the highest sharpness but also the highest noise level, with a noise value of 147.418 $HU^2 \cdot mm^2$ at a frequency of 0.972 mm^{-1} for 10 mAs. At 30 mAs, the highest recorded noise level is 63.430 $HU^2 \cdot mm^2$ at a frequency of 0.757 mm^{-1}, while at 50 mAs, the highest noise level is 54.391 $HU^2 \cdot mm^2$ at a frequency of 0.765 mm^{-1}.

A slice thickness of 5 mm provides lower sharpness but also results in reduced noise levels at nearly the same frequency as a 1 mm slice thickness. As slice thickness increases, noise levels decrease across all frequencies, indicating that thicker slices result in slightly smoother image textures. Additionally, as mAs increase, noise levels and frequencies decrease at all slice thicknesses, suggesting that higher mAs lead to smoother image textures.

In general, thicker slices produce images with lower noise levels, while thinner slices result in higher noise levels. Increasing slice thickness tends to reduce resolution, which may lead to diagnostic errors [26,27]. Conversely, reducing the tube current (mAs) increases image noise, potentially obscuring anatomical details and lowering the detection of small lesions. NPS provides data on noise texture at each frequency.

The NPS measurements on a phantom with slice thickness ranging from 1 mm to 5 mm show that thicker slices produce lower noise, while thinner slices result in higher noise. Slice thickness is selected based on the examination purpose and the type of pathology being assessed. Thin slices are commonly used for examinations requiring the detection of small structures, such as head scans, bone trabeculae, breast microcalcifications, contrast-enhanced vessels, and lung cancer screening [28-30].

Table 1. Results of NPS analysis with varying slice thickness, mAs, and type of kernel.

mAs	Slice Thickness (mm)	Average Frequency	Noise	Kernel
10	1	0.972	147.418	L
	2	1.027	139.555	
	3	1.046	137.377	
	4	1.055	135.983	
	5	1.061	136.011	
30	1	0.757	63.430	L
	2	0.812	52.224	
	3	0.838	48.642	
	4	0.866	46.505	
	5	0.873	45.876	
50	1	0.765	54.391	L
	2	0.828	44.143	
	3	0.843	43.418	
	4	0.875	40.811	
	5	0.886	40.312	
200	1	0.148	11.208	B
	2	0.132	10.207	
	3	0.137	10.836	
	4	0.125	12.072	
	5	0.167	6.289	

A study by Raharja et al. revealed that NPS results are influenced not only by slice thickness but also by variations in reconstruction kernel type [31]. A numerical analysis of NPS results with different kernel types is presented in Table 1. According to Table 1, sharp-detail kernels provide the highest sharpness but produce the highest noise level, reaching 147 $HU^2 \cdot mm^2$ at a frequency of 0.972. In contrast, smooth kernels have lower sharpness with a noise value of 6 $HU^2 \cdot mm^2$ at a frequency of 0.167.

The kernel type can be defined as a digital image reconstruction technique used to enhance image quality by reducing noise [32]. Different CT imaging systems may use varying terms for digital image reconstruction techniques. In CT diagnosis, reconstruction kernels play a crucial role, as the choice of kernel affects spatial resolution and noise levels. Sharp kernels can improve image quality by enhancing detail visibility [33].

The purpose of using kernels is to enhance clinical diagnostic accuracy by adapting to the characteristics of the examined object. It is well known that high-spatial-resolution (sharp) kernels provide greater detail but also produce higher noise levels. In contrast, low-resolution (smooth) kernels generate images with lower spatial resolution and reduced noise levels [34].

According to a study by Monnin et al., kernels are used to enhance clinical diagnostic accuracy by considering the characteristics of the examined object. It is well known that smooth kernels are commonly used for soft tissue assessments, such as detecting abnormalities in the brain, mediastinum, neck, and nasopharynx. In contrast, sharp kernels are used to enhance the edges of organs or tissues with low contrast, such as in bone examinations [35].

Most CT manufacturers offer low-dose solutions with good image quality for lung scanning, based on reconstruction types. However, these methods are less efficient due to high costs, long scan times, and complexity [36-40]. In short, Model-Based Iterative Reconstruction (MBIR) effectively reduces dose but is considered time-inefficient [41].

In this study, optimizing lung cancer lesion detection using standard-dose and low-dose scanning was achieved efficiently and feasibly by adjusting scan parameters such as mAs, pitch, and kernel to achieve a low dose with good image quality. However, this study also has some limitations.

First, all images were reconstructed using the Filtered Back Projection (FBP) method, preventing an analysis of the relationship between reconstruction type and image quality in the in-house phantom. This limitation is due to the use of an older-generation CT scanner that still relies on traditional reconstruction techniques. As a result, image quality optimization was limited to adjusting scan parameters based on the examination purpose. Second, no subjective evaluation was conducted involving specialist doctors or radiology experts.

CONCLUSION

The designed phantom effectively demonstrates the capability to compare standard-dose and low-dose CT scanning for detecting lung cancer lesions using practical, efficient, and clinically feasible parameters. The results indicate that low-dose scanning can detect small lesions (<3 mm) with Hounsfield Unit (HU) values similar to lung tissue, while maintaining high contrast differences (SDNR $\geq$ 5), optimal Figure of Merit (FOM), and well-characterized Noise Power Spectrum (NPS) across various slice thicknesses, reconstruction kernels, and mAs settings. Noise levels were found to decrease with increasing slice thickness and mAs, whereas sharp reconstruction kernels designed to enhance object boundaries resulted in higher noise.

ACKNOWLEDGMENT

The authors would like to express their sincere gratitude to the Radiology Department of MRCCC Siloam Hospital for their valuable support and assistance during data collection and image acquisition. Their collaboration and technical expertise greatly contributed to the success of this study.

AUTHOR CONTRIBUTION

Conceptualization: L. E. Lubis, D. S. Soejoko, Methodology: A. K. Hutami, L. E. Lubis, D. S. Soejoko, Data Collection: A. K. Hutami, H. D. R. Rahaja, Data Analysis: A. K. Hutami, L. E. Lubis, D. S. Soejoko, Writing - Original Draft: A. K. Hutami, Writing – Review & Editing: H. D. R. Rahaja, L. E. Lubis, D. S. Soejoko

REFERENCES

1. WHO, Total #Cancer Cases (2018), 2020. https://www.who.int/publications/m/item/cancer-idn-2020. Retrieved in March 2024
2. C. McCollough, D. Cody, S. Edyvean *et al*., Report No. 96, The Measurement, Reporting, and Management of Radiation Dose in CT, American Association of Physicists in Medicine (AAPM), College Park (2008) 1.

3. R. Meza, J. Jeon, I. Toumazis *et al*., JAMA **325** (2021) 988.
4. L. Manuel, L.S. Fong, T. Ly *et al*., Interact. Cardiovasc. Thorac. Surg. **33** (2021) 741.
5. C. Goudemant, V. Durieux, B. Grigoriu *et al.*, Rev. Mal. Respir. **38** (2021) 489.
6. M. Reck, S. Dettmer, H.-U. Kauczor *et al*., Dtsch. Arztebl. (2023) 387.
7. H. L. Lancaster, M. A. Heuvelmans, and M. Oudkerk, J. Intern. Med. **292** (2022) 68.
8. R. M. Hoffman, R. P. Atallah, R. D. Struble *et al.*, J. Gen. Intern. Med. **35** (2020) 3015.
9. Council NR., Beir VII: Health Risks from Exposure to Low Levels of Ionizing Radiation. https://nap.nationalacademies.org/resource/11340/beir_vii_final.pdf. Retrieved in December 2024.
10. S. Iranmakani, A. R. Jahanshahi, P. Mehnati *et al*., J. Med. Signals. Sens. **12** (2022) 64.
11. G. L. Zeng, J. Radiol. Imaging **4** (2020) 45.
12. B. Jiang, N. Li, X. Shi *et al.*, Radiol. **303** (2022) 202.
13. P.G. Mikhael, J. Wohlwend, A. Yala *et al*., J. Clin. Oncol. **41** (2023) 2191
14. J. A. Yeom, K. U. Kim, M. Hwang *et al.*, Medicina (Lithuania) **58** (2022) 939.
15. L. E. Lubis, I. Hariyati, D. Ryangga *et al*., Atom Indones. **46** (2020) 69.
16. Y. Niu, S. Huang, H. Zhang *et al.*, Quant. Imaging. Med. Surg. **11** (2021) 380.
17. J. Greffier, Y. Barbotteau, and F. Gardavaud, Diagn. Interv. Imaging **103** (2022) 555.
18. J. T. Bushberg, J.A. Siebert, E. M. Leidholdt *et al.*, The Essential Physics of Medical Imaging, Wolters Kluwer Health / Lippincott Williams & Wilkins, Pennsylvania (2012).
19. J. B. Solomon, X. Li, E. Samei, Am. J. Roentgenol. **200** (2013) 592.
20. P. J. Mazzone, G. A. Silvestri, L. H. Souter *et al*., CHEST **160** (2021) e427.
21. K. Ichikawa, T. Kobayashi, M. Sagawa *et al*., J. Appl. Clin. Med. Phys. **16** (2015) 1.
22. M. E. Widiatmoko and S. Ramadanti, Jurnal Kesehatan Vokasional **8** (2023) 174. (in Indonesian)
23. K. M. Ogden, W. Huda, M. R. Khorasani *et al*. *A Comparison of Three CT Voltage Optimization Strategies*, in: Proceedings of SPIE **6913** (2008) 691351-1.
24. E. Seeram, Computed Tomography: Physical Principles, Clinical Applications, and Quality Control, Saunders, St. Louis (2016).
25. Priyanka, R. Kadavigere, and S. Sukumar, Clin. Neuroradiol. **34** (2024) 229.
26. M. Alshipli and N. A. Kabir, J. Phys.: Conf. Ser. **851** (2017) 012005.
27. J. M. Ford and S. J. Decker, J. Forensic. Radiol. Imaging **4** (2016) 43.
28. S. C. Bushong, Radiologic Science for Technologists: Physics, Biology, and Protection, Mosby; St. Louis, Missouri **(**2021).
29. O. Ekizoglu, E. Inci, E. Hocaoglu *et al*., J. Craniofac. Surg. **25** (2014) 957.
30. J. Wu, R. Li, H. Zhang *et al*., Thorac. Cancer **15** (2024) 1522.
31. H. D. R. Raharja, D. Putra, A. Naufal *et al*., *Noise Power Spectrum (NPS) Characteristics on CT Imaging: Slice Thickness and Filter Types Variations*, in: Proceedings of the 21st South-East Asian Congress of Medical Physics (SEACOMP) and 6th Annual Scientific Meeting on Medical Physics And Biophysics (PIT-FMB), AIP Publising (2024) 030014.
32. J. Choe, S. M. Lee, K. H. Do *et al*. Radiology **292** (2019)
33. H. Lang, J. Neubauer, B. Fritz *et al*., Eur. Radiol. **26** (2016) 4551.
34. M. Chillarón, V. Vidal, and G. Verdú, PLoS One **15** (2020) e0229113.
35. P. Monnin, A. Viry, F. R. Verdun *et al*., Phys. Med. Biol. **65** (2020) 105009.
36. M. Afadzi, E. K. Lysvik, H. K. Andersen *et al*., Eur. J. Radiol. **114** (2019) 62.
37. J. Gariani, S. P. Martin, D. Botsikas *et al*., Br. J. Radiol. **91** (2018) 20170443.
38. T. Kubo, Y. Ohno, M. Nishino *et al*., Eur. J. Radiol. Open **3** (2016) 86.
39. A. Ruano-Ravina, M. Pérez-Ríos, P. Casàn-Clará *et al*., Lancet Oncol. **19** (2018) e131.
40. H. Shen, Front. Med. **12** (2018) 116.
41. S. Park, J. H. Yoon, I. Joo *et al*., Eur. Radiol. **32** (2022) 2865.